Research Article | Vol. 15, No. 12 / 1 Dec 2024 / Biomedical Optics Express 6940
Biomedical Optics EXPRESS

Spatial polarimetric second harmonic generation evaluation of collagen in a hypophosphatasia mouse model

TIANYI ZHENG,[1,†] EMILY G. PENDLETON,[2,†] RUTH P. BARROW,[2] ANA D. MASLESA,[2] PETER A. KNER,[1] AND LUKE J. MORTENSEN[2,3,*]

[1]School of Electrical and Computer Engineering, University of Georgia, Athens, GA 30602, USA
[2]Regenerative Bioscience Center, Rhodes Center for ADS, University of Georgia, Athens, GA 30602, USA
[3]School of Chemical, Materials and Biomedical Engineering, University of Georgia, Athens, GA 30602, USA
[†]Co-first author
[*]Luke.Mortensen@uga.edu

Abstract: Polarization-resolved second harmonic generation (pSHG) is a label-free method that has been used in a range of tissue types to describe collagen orientation. In this work, we develop pSHG analysis techniques for investigating cranial bone collagen assembly defects occurring in a mouse model of hypophosphatasia (HPP), a metabolic bone disease characterized by a lack of bone mineralization. After observing differences in bone collagen lamellar sheet structures using scanning electron microscopy, we found similar alterations with pSHG between the healthy and HPP mouse collagen lamellar sheet organization. We then developed a spatial polarimetric gray-level co-occurrence matrix (spGLCM) method to explore polarization-mediated textural differences in the bone collagen mesh. We used our spGLCM method to describe the collagen organizational differences between HPP and healthy bone along the polarimetric axis that may be caused by poorly aligned collagen molecules and a reduction in collagen density. Finally, we applied machine learning classifiers to predict bone disease state using pSHG imaging and spGLCM methods. Comparing random forest (RF) and XGBoost technique on spGLCM, we were able to accurately separate unknown images from the two groups with an averaged F1 score of 92.30%±3.11% by using RF. Our strategy could potentially allow for monitoring of therapeutic efficacy and disease progression in HPP, or even be extended to other collagen-related ailments or tissues.

1. Introduction

Second harmonic generation (SHG) imaging is a nonlinear technique sensitive to non-centrosymmetric molecules like type 1 collagen, which is abundant in structural tissues in the body. Expressed in numerous organ systems, type 1 collagen undergoes modifications and assembly into secondary structures in each location to provide tissue-specific mechanical and biochemical properties. Therefore, tissue defects in the assembly and modification of collagen structures may result from disease pathology, which could in turn be detected using SHG imaging [1].

Bone collagen has extensive secondary modifications during mesh formation and co-deposition with crystalline hydroxyapatite mineral. Collagen fibrils are produced early in osteoblastic differentiation, and with the assistance of mineral seeds self-assemble in the extracellular space [2]. As bone formation progresses, matrix vesicles rich in the enzyme tissue non-specific alkaline phosphatase (TNALP) mediate mineral deposition at the surface of cells and throughout collagen fibers where the extracellular matrix vesicles accumulate [3]. These mineral deposits within and between collagen fibers significantly strengthen the toughness, failure strain and strength of the

#529428 https://doi.org/10.1364/BOE.529428
Journal © 2024 Received 7 May 2024; revised 24 Jul 2024; accepted 27 Jul 2024; published 22 Nov 2024

Biomedical Optics EXPRESS

bone [4–6]. The mineral binds together with the collagen using a combination of physical linkages [5], direct interactions with TNALP [7–10], hydrogen bonds [11], electrostatic forces [12], salt bridges [11], and polysaccharide binding [13]. Together these interdependent mineralized fibrillar structures create a hierarchy of lamellar sheets that increase the ability of bone to withstand torsion and tension. The lamellar sheets self-assemble on top of one another in a plywood-like fashion with neighboring layers arranged at differing angles.

Prior work by our group [14] and others [15] has used a SHG approach to explore the organization of bone lamellar structures to uncover guiding principles of bone collagen organization. SHG is non-destructive and provides direct information about collagen structure without the need for fluorescent labeling. When imaged using polarized incident light, SHG can increase contrast to highlight collagen orientation within tissues [16]. The intensity of the SHG signal is dependent on the second order susceptibility χ (2), which is the bulk quantity visualized in the SHG microscope and relies on collagen orientation relative to the excitation light and collagen abundance. Second order susceptibility is associated with the molecular order of collagen and the coherent amplification of peptide bonds along the length of the molecule. This is defined by the first hyperpolarizability β [1], which is due to the coherent amplification of the SHG signals from the peptide bonds aligned along the length of the collagen molecule [17].

This work aims to build on our prior efforts with SHG polarimetry in bone [14] to evaluate the collagen lamellar sheet formation in a mouse model of a metabolic bone disorder impacting mineral deposition. Hypophosphatasia (HPP) is a rare metabolic bone disease characterized by mutations in the ALPL gene that encodes for TNALP [18,19], which is critical for mineral production in bone [20]. TNALP is present on the surface of bone forming cells and their mineralizing matrix vesicles and, along with associated annexins [7], allows these vesicles to bind to collagen and deposit mineral crystals [9]. Therefore, bones with reduced TNALP activity are likely to have an impaired capacity to form mineral stabilizing links between collagen molecules and may suffer from impaired assembly of collagen into larger lamellar sheet structures. HPP is characterized by rickets in children and osteomalacia in adults [21], with patients prone to fractures [3]. Although the characteristic diminished mineral content of the bone in HPP is associated with a reduction in bone forming cells in the growth plate and in overall bone size [23], the impact of HPP on collagen structure has not been characterized previously.

In this work, we use polarization-resolved SHG to investigate HPP disruption of collagen assembly. We determine the dominant orientation of collagen fibers within each pixel to delineate lamellar sheets. We find that the HPP lamellar sheets are significantly smaller and less well defined than the wild type (WT) lamellar sheets, which may contribute to the overall weakness of HPP bone. We then use the gray-level co-occurrence matrix (GLCM) to describe the texture of the SHG images and quantify differences in collagen organization induced by HPP. We explore a spatial polarimetric GLCM method (spGLCM) which incorporates the response of the pixel of interest and its neighbors along the polarization angle axis to yield an additional component to the texture. Compared to standard GLCM, spGLCM increases sensitivity to the bone collagen structure, finding significant alterations in the collagen of diseased HPP mice using several well accepted machine learning techniques including random forest (RF) and XGBoost to classify the state of disease. This implementation of SHG polarimetry analysis could be used as a guide for researchers to describe bone health, disease progression, and response to therapy. Our findings could enable future strategies for label-free identification of disease states of the bone and monitor effectiveness of therapies for bone disorders like HPP; or be extended to study other metabolic bone disorders.

Biomedical Optics EXPRESS

2. Methods

2.1. Animals

The use of all animals in this study was approved by The University of Georgia Institutional Animal Care and Use Committee. Alpl-/- mice mimic infantile HPP, with phenotypes of elevated levels of inorganic pyrophosphate (PPi), a lack of mineralization, and end-stage seizures. All mice were given free access to modified laboratory rodent diet 5001 with 325 ppm Pyridoxine to delay seizures and extend lifespan. Knockout Alpl-/- mice were identified by PCR at birth (Day 0) in accordance with a protocol developed by Jackson Laboratory (Bar Harbor, ME) using primers 5' – CCGTGCATCTGCCAGTTTGAGGGGA – 3', 5' – CTGGCACAAAAGAGTTGGTAAGGCAG – 3', 5' – GATCGGAACGTCAATTAACG TCAAT – 3'. Both Alpl+/+ and Alpl-/- mice were collected at P14 (postpartum day 14) because in this disease model mice begin to die by P16 with 100% mortality by P21. The skulls of the specimens were extracted, and the cranial cavity was evacuated. Specimens were mounted in silicone to prevent movement and hydrated with PBS throughout imaging. A total of 26 mice (13 wild type (WT), 13 HPP) were sacrificed and 5 images per mouse of the intact cranial bone were captured within the approximate region indicated by the blue square in Fig. 2(A).

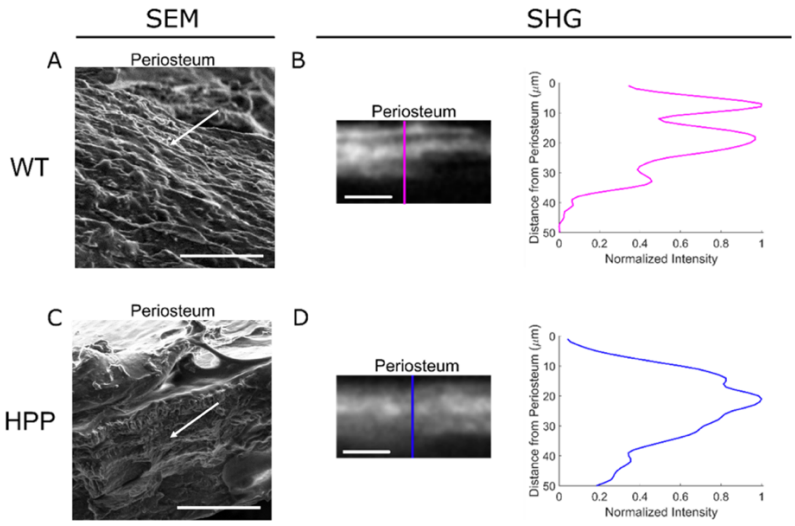

Fig. 1. SEM and SHG imaging show structural lamella sheets differences between wild type and HPP bone. The lamellar sheets of a two-week-old wild type (WT) mouse are organized in a parallel fashion and can be visualized with SEM (A) and SHG (B). The skull of a two-week-old HPP mouse has lamellar sheet defects that appear smaller in size and irregular in organization (C, D). Scale bar indicates 20 μm.

2.2. Optical setup

The optical setup is similar to what we have reported previously [14,24]. Briefly, it has a Ti:Sapphire femtosecond pulsed laser that produces light from 680 nm to 1080 nm—we used 775 nm, with the power of the beam adjusted by a half wave retarder and polarizing beam splitter, then rapidly modulated by a Pockels cell attenuator and scanned over the specimen. The back-collected emission light is sent to a photon multiplier tube with a 409 nm long-pass dichroic beam splitter and bandpass filter of 390/18 to capture SHG of collagen. SHG intensity is dependent on angular matching between laser polarization and fiber alignment, which can be exploited to enhance contrast of collagen fibers [25]. Therefore, SHG images (512×512 pixels,

Biomedical Optics EXPRESS

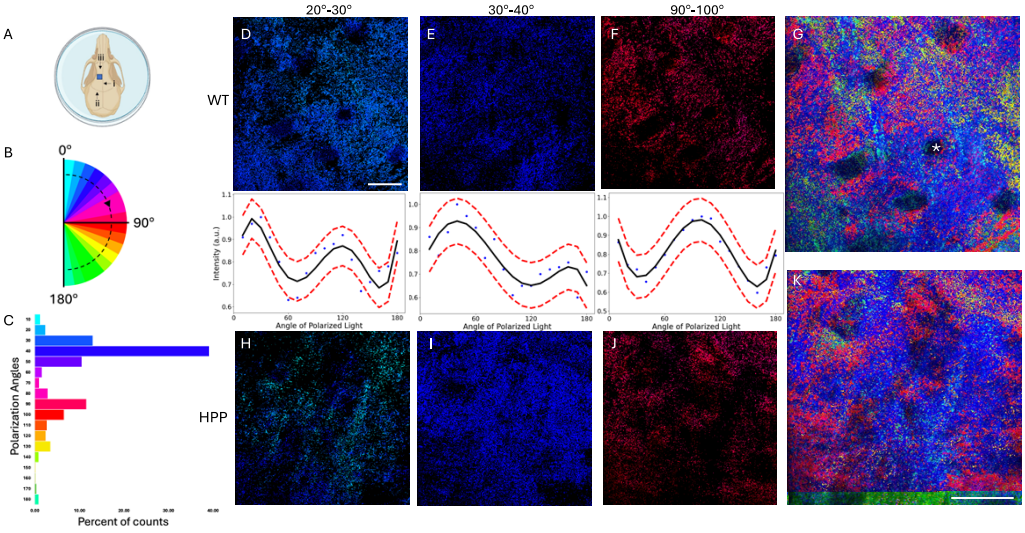

Fig. 2. SHG polarized imaging identifies collagen structures in WT and HPP bone. (A) The frontal bones of juvenile mice were imaged dorsal to the jugum limitans (i) and lateral to the sagittal suture (ii). (B) Polarized light was rotated, images were collected every 10°, and pixels containing collagen fiber information were assigned colors based on fiber orientation. (C) histogram of the angular distribution illustrates three specific orientations were chosen. Regions of similar orientations are seen in the WT calvaria (D-G) while the HPP calvaria has a mixture of orientations throughout the viewing area (H-K). The asterisk in G denotes an osteocyte lacuna. Scale Bar: 20 µm. Average intensity profiles were plotted (blue dots), fitted (black line), and 95% confidence intervals (red dashed lines) were established to demonstrate the intensity signature of each orientation.

FOV 52.06 × 52.06 µm) were collected with linearly polarized excitation, using a half-waveplate rotated at 5° intervals to evaluate collagen orientation within the focus. We evaluated polarization quality with a polarization state analyzer to measure the Stokes parameters at each excitation angle and correct any residual polarization distortion. The polarization was verified to be maintained at the focus by imaging spherical T-cells labeled with Di-8-ANEPPS [25,55]. Representative polarized stacks of each mouse skull were generated at 5, 10, and 15 µm of depth. To probe differences between HPP and WT mice, 5 distinct regions of the calvaria of each mouse 5 µm from the periosteum were imaged to create polarized image sets. For all mice, the region lateral to the sagittal suture, anterior to the coronal suture, and posterior to the jugum limitans of the whole cranial bone was imaged (see Supplement 1 s1). We compensated for average intensity variations between excitation polarizations in the images using the variant part of average intensity of all SHG raw images.

2.3. Scanning electron microscopy

To perform independent analysis of lamella sheet organization, we used scanning electron microscopy (SEM) to image skull fractured edges in WT and HPP bone. Fresh skulls were snap frozen and freeze fractured before dehydration in a vacuum. Samples were then carbon coated and mounted for SEM analysis with a Zeiss 1450EP.

2.4. Angular distribution of collagen fibers

To determine the approximate orientation of collagen fibers within the excited volume, we used a single linear polarization of excitation light that was rotated at 5° intervals from 0 to 180

Biomedical Optics EXPRESS

degrees to generate polarimetric, epi-collected second harmonic signal [14]. The second-order susceptibility, linked to collagen's molecular order, amplifies the molecular SHG signals of peptide bonds coherently along the molecule's length. These signals predominantly align at approximately 50° from the collagen molecule's triple helix of alpha-chains, which is aligned along the main axis of the collagen fiber. A mathematical model was used to fit the relative collagen second-order susceptibility tensors χ to the measured experimental values [26]. The intensity of the SHG signal is dependent on the electric field, the number of collagen fibers within the focal volume, and the orderliness of the collagen fibers. We assume a more general form of the χ tensor that considers both trigonal and cylindrical symmetry. Therefore, the resulting P-SHG signal can be described as:

$$I^{2\omega}(\alpha) = A[(\chi_{yyy}sin^2(\alpha-\varphi) + \chi_{xxz}sin^2(\alpha-\varphi))^2 + (\chi_{zxx}sin^2(\alpha-\varphi) + \chi_{zzz}cos^2(\alpha-\varphi))^2] \quad (1)$$

where χ_{yyy}, χ_{xxz} , χ_{zxx} , χ_{zzz} are susceptibility tensors χ, A is the average number of detected photons, α is the polarization orientation of the excitation light, and φ is a measure of the average collagen fiber orientation within the focal volume [27]. $S = |\chi(2)yyy|/\chi(2)zxx$ was calculated to describe the balance between trigonal and cylindrical symmetries [26]. The nonlinear susceptibility ratio ρ = χ(2)xxx/χ(2)xyy was also calculated and compared to ratio values reported for collagen in the literature (~1.4 for hydrated collage [n) [28]. To visualize collagen lamellar orientation and organization, ImageJ2 and Python (version 3.8.12) were used. To form the color images, every 10° of collagen orientation was assigned a different color, with the collagen fibers parallel to the sagittal suture deemed 0°.

2.5. Delineation of collagen sheet boundaries

We next sought to describe boundaries of collagen lamella sheets 5 μm, 10 μm, and 15 μm from the periosteum using 2D images with the calculated angle of collagen orientation assigned to each pixel. The standard deviation of the angular differences between each pixel and its nearest eight neighbors was calculated. We used a small region of interest for this calculation to determine similarities of neighboring collagen molecules that would likely be within the same fiber or within the same lamella sheet. A high standard deviation is therefore expected at the boundaries of lamellar sheets that have juxtaposed angles of orientation or within a region of poorly aligned fibers. The average SHG intensity image was masked using the Otsu technique and overlaid on the standard deviation image. We observed a drop in SHG signal with most HPP samples when compared to the WT bone and differences in the amount of SHG signal due to collagen composition and bone structure (i.e. osteocyte lacunae). Therefore, an automated Otsu threshold for each image was used rather than a single threshold value for all images.

2.6. Spatial polarimetric GLCM analysis

SHG polarimetry is known to provide contrast for the examination of secondary collagen structures and has been used in the visualization of bone lamellar sheets [14,15,29]. Polarimetry utilizes alterations in light polarization to reveal hidden structural organization within collagen structures, offering enhanced contrast and insights into orientation and properties. To minimize measurement variance based on physical orientation, we oriented all skulls in the same direction such that the nose of the mouse was towards the top of the image, which yielded the dominant direction of collagen fibers to be along the y-axis of the final image. We then captured an image using each of excitation light polarization directions to create a polarized image stack. To leverage the polarization contrast, we performed second order texture analysis across x, y, and polar dimensions using a modified form of the symmetric gray level co-occurrence matrix (GLCM) [30] in Python which we term spatial-polarimetric gray level co-occurrence matrix (spGLCM),

Biomedical Optics EXPRESS

adapted from previously published approaches using 3-dimensional stacks for GLCM analysis [31]. Our final calculation of the spGLCM values in each polarimetric image are expressed as GLCM analysis of the corrected polarization-resolved SHG raw images along 4 different axes (Supplement 1 s2). Compared with 2D GLCM algorithms, the spGLCM method incorporates the additional polarization contrast to provide improved discrimination of the alignment of collagen fibers and their organization into lamellar sheet structures.

2.7. Machine learning analysis

Data analysis was performed with Python (version 3.8.12). To investigate separation between experimental groups based on spGLCM measurements, we conducted RF and XGBoost techniques. In all methods, 121 spGLCM measurements for 13 mice per group with 5 images per mouse. We applied rotational symmetry to the spGLCM features along the polarization axis to yield mirrored data from 0°-180° to 180°-360°. Then 80% data is used for training and 20% data is used for 5-fold cross validation. Once computed, F1 score is used to measure the classification accuracy.

3. Results

3.1. Visualization of collagen sheets

To visualize collagen sheets, we freeze fractured calvaria of WT and HPP bone separately and performed SEM imaging at the fracture site to create a transverse view of the bone edge. We are clearly able to visualize the lamella sheet formations in some subregions of WT bone along the fracture line (Fig. 1(A)) compared with HPP (Fig. 1(C)), as indicated by the white arrow. The HPP bone, however, has disrupted lamellar sheet formation in some subregions with small collagen formations undulating in the cortical region of the skull with gapping between the layers (Fig. 1(C)). This results in a lack of well-defined sheets and a large region of unorganized collagen structures.

We then attempted to visualize the same phenomenon with SHG. SHG images were generated by using a single excitation polarization and raster scanning in the x-y dimension, then creating a z-stack with 1 μm step size, before finally reconstructing and reslicing with a 50 μm projection in the y dimension to yield an x-z image of the bone. While SEM accentuated boundaries between physically bonded areas, optical SHG cross-sections specifically target collagen molecules in a sample. The SHG x-z cross-sections find alternating regions of bright and dark collagen intensity profiles suggesting alternating layers of differently ordered collagen that are consistent with lamella sheet structures (Fig. 1(B)). For HPP bone, however, the collagen intensity was more similar throughout the image, suggesting a perhaps reduced definition of lamella sheet structures (Fig. 1(D)).

3.2. Angular distribution of collagen fibers in bone

Using Eq. (1), the dominant angle of collagen fiber orientation, φ, of each pixel was determined and every 10° was assigned a representative color (Fig. 2(B)). The WT bone displays subregions (light blue and red pixels) that are localized in well-defined regions especially around suspected osteocytes, indicating several well aligned groups of fibers (Fig. 2(D) & (F)) as well as a dominant orientation for the field of view (Fig. 2(E)). Display of the whole spectrum of fiber orientations (Fig. 2(G) & (K)) suggests that in comparison with WT, the HPP bone has fibers of similar orientation but seems to have reduced small regions of similar orientation. The histogram of the angular distribution (Fig. 2(C)) illustrates three specific orientations (20°-30°, 30°-40°,90°-100°) that were chosen for individual display to highlight the main orientations present in the sample and their respective polarization response curves (Fig. 2(D-F), (H-J)).

Biomedical Optics EXPRESS

3.3. Lamella sheet integrity

After visualizing collagen assembly, we sought to more closely investigate boundaries of collagen organization into lamella sheet-like regions. To do so, we acquired polarimetric images and determined φ at 5 µm, 10 µm, and 15 µm depth into the bone, measured from the periosteum. To quantify the similarity between pixels and their neighbors, we first determined the angle of orientation of each pixel, measured the standard deviation (SD) and then found the average difference in orientation between a pixel of interest and its nearest eight neighbors. In randomly selected example WT bones, we find regions with highly conserved angular directions of collagen fibers (red regions, Fig. 3(A)-(C)); and formation of collagen sheet-like structures oriented in different directions around osteocyte lacunae. These findings suggest that the HPP bone has reduced regions of well-defined lamella, with collagen fibers that are more heterogeneously distributed relative to nearby fibers (Fig. 3(D)-(F)). We then quantified the distribution of these SD values (Fig. 3(G)-(L)) using a cumulative distribution function (CDF). In this representative plot, the CDF for WT bone increases more rapidly than for HPP bone. This suggests that the WT bone tends to have lower SD values, which would indicate more similar spatial distributions of collagen compared to HPP bone.

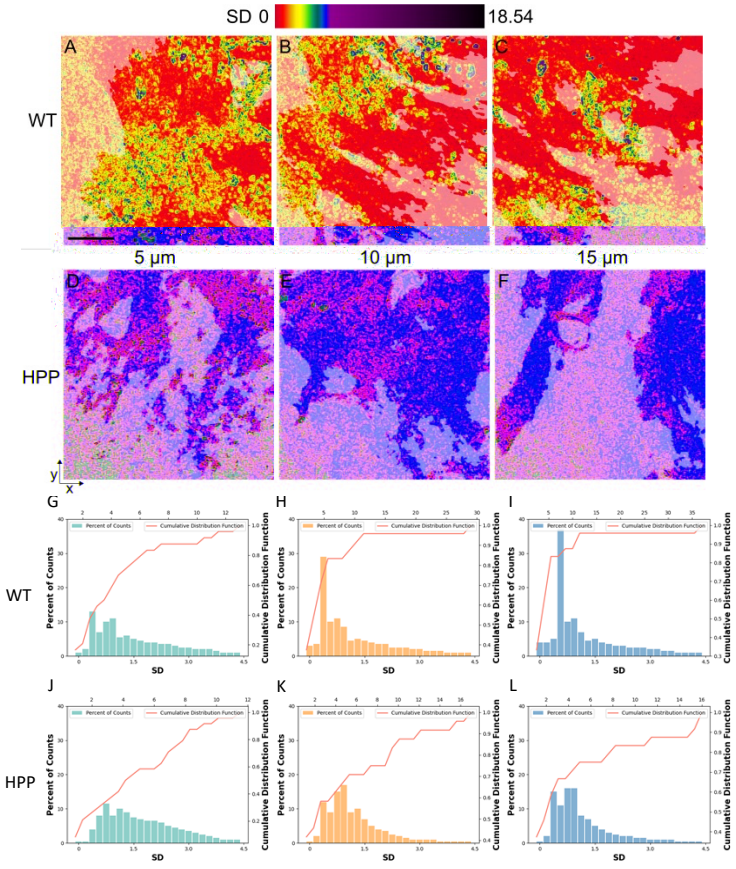

Fig. 3. Local variance of collagen orientation in WT (A-C) and HPP (D-F) bone were evaluated at 5 µm (A, D), 10 µm (B, E), and 15 µm (C, F) from the periosteum. Well aligned areas (red) are prominent in the WT bone and are smaller in the HPP bone. WT histograms (G-I) are left-skewed while the distribution of the HPP histograms (J-L) are more normally distributed. Scale bar 20 µm.

Biomedical Optics EXPRESS

Furthermore, we analyzed the polarization data using a general symmetry model presented in Eq. (1) [28,32,33] and then compared parameter ρ and S. The nonlinear susceptibility ratio $\rho \approx 1.2 \pm 0.04$. Then, we compared ρ values obtained at different depths suggesting that effects resulting from imaging depth (e.g. birefringence) do not significantly affect pSHG measurements at less than 15 μm depth. Supplement 1 s3 shows the maximum intensity projections of pSHG image stacks acquired in WT and HPP. WT samples are characterized by collagen fiber bundles generated from multiple orientations, resulting in relatively high symmetry parameter S values, with an average of 0.90 ± 1.26. In contrast, HPP specimens lack proper collagen formation and are characterized by collagen fibrils assembled from a single orientation, akin to a straight-aligned collagen fibril bundle, with an average S value of 0.26 ± 0.32.

3.4. Spatial polarimetric GLCM analysis

We next explored the grey level variations in polarization-resolved SHG to examine the effects of HPP on bone organization. To accomplish this, we developed a spatial polarimetric GLCM analysis (spGLCM) that incorporates polarization contrast into texture analysis. spGLCM measures included energy, homogeneity, contrast, entropy and correlation with offsets ranging from 1 to 17 pixels along x-axis, y-axis, polar-axis and polar-spatial diagonal axis. For this analysis, we imaged 13 mice per group with 5 image stacks each at a depth of 5 μm from the surface. To demonstrate how the WT and HPP images respond to spGLCM measures, the GLCM parameters were extracted from a representative image from each group and plotted to provide a visualization of observed trends with different offsets along each analysis direction (Fig. 4). The heatmap is generated to evaluating the difference between spGLCM features of WT and HPP. To generate this heatmap, we measure the difference between the mean values of five features (entropy, homogeneity, contrast, correlation and energy), along four directions (polar, x, y, diagonal) at nine different offsets (1,3,5,7,9,11,13,15,17) of 121 WT and HPP samples separately.

Energy is a measure of the degree of stability of the gray scale variations, which reflects the degree of uniformity of the image. We observed small trends towards a difference between the two groups when we compare energy values in the spatial dimension at different offsets along the x-axis and y-axis (orange and green lines). Along the polarization axis and diagonal axis (blue and red line) the energy values tend to stay higher in the HPP than the WT even at extended offsets. The difference is pronounced for spGLCM measurement within 100° to 170° (offset between 10 to 17) when compared to the WT energy values, indicating a higher degree of stability of the gray scale variation within sampled fibers (i.e. more uniformity in the polar dimension) that is also present in the diagonal dimension in a slightly reduced fashion in the HPP image.

Homogeneity describes local changes of image texture, indicating similarities of gray level distributions. Overall, in the spatial dimension along the x-axis and y-axis the WT and HPP images have similar homogeneity measures across offsets, with some differences observed with pixels of interest that are in close proximity. Along the polarization and diagonal axes the WT and HPP images have a qualitatively somewhat different rate of change between 90° to 170° (offset between 9 to 17). This suggests that the gray levels within sampled collagen pixels differ from one another more quickly in the HPP image, indicating that the texture is less uniform and collagen orientation with a single pixel is more varied.

Contrast measures the variance between the pixels of interest, which highlights edges of features. In the spatial dimension along the x-axis and y-axis, the overall shape of the contrast measure is similar between the WT and the HPP representative images, and the rate of change in the contrast measure is also similar. However, the contrast values of the WT image are overall higher than in the HPP image. Along the polarization and diagonal axes, the contrast values of the WT image are much higher than the HPP image, especially after 100° (offset > 10), indicating

Biomedical Optics EXPRESS

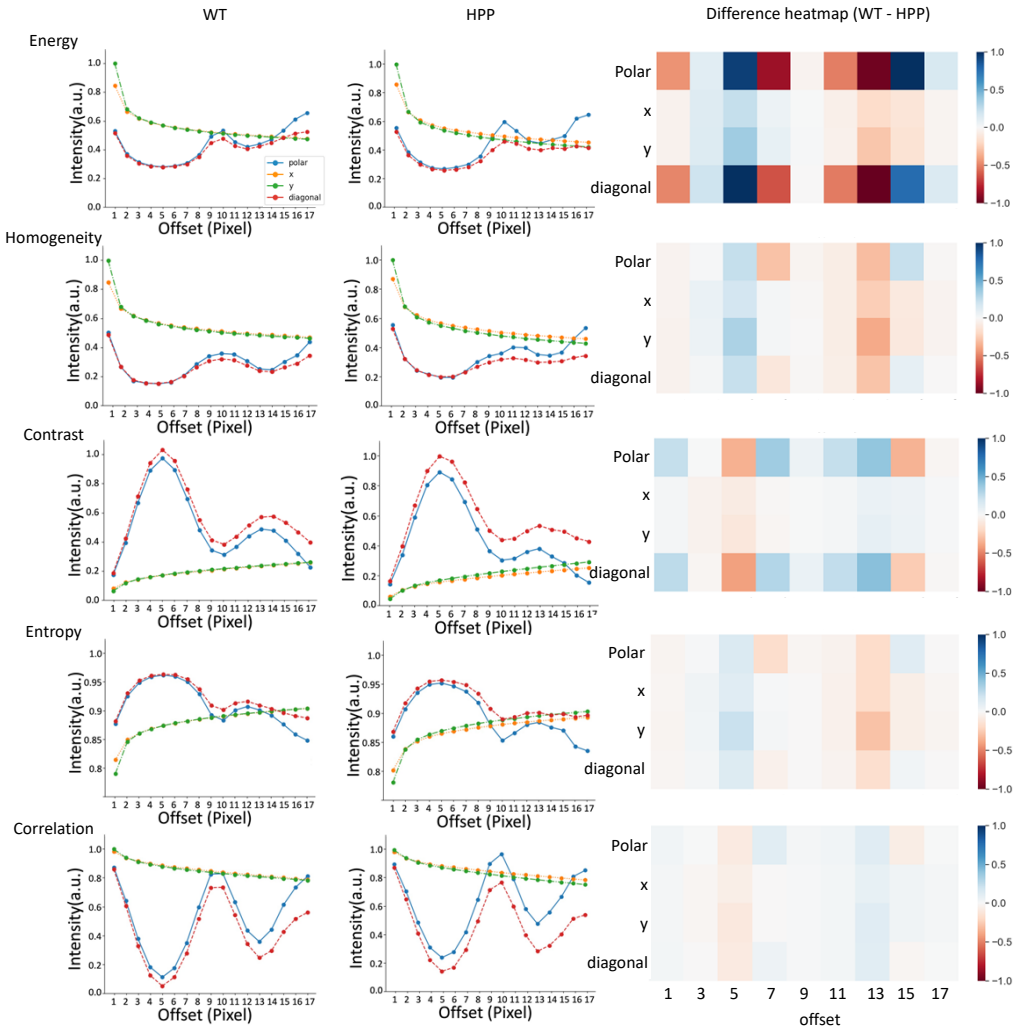

Fig. 4. spGLCM metrics describe the differences between example WT and HPP polarization-resolved SHG images. A single polarization-resolved SHG image of WT and HPP bone was analyzed with spGLCM to exemplify the differences between the measures of contrast, homogeneity, energy, entropy and correlation at four exemplary directions. A heatmap was generated to visualize the average difference in all 121 WT and HPP images. The GLCM measurements at differing pixel offsets along the x- and y-axes responds similarly in WT and HPP, but with different magnitudes. However, measurements along the polar-axis and diagonal-axis suggest a potential difference between WT and HPP with oscillations due to collagen contrast in the polar dimension, indicating sensitivity to the texture differences caused by polarization.

Biomedical Optics EXPRESS

more distinct edges of collagen fiber formation in the WT image and more homogeneous gray levels in the HPP image, suggesting a lack of collagen fiber organization or less ordered collagen.

Entropy measures the level of disorder or uncertainty in the grayscale variations within the images, which could highlight randomness or lack of clear patterns within the grayscale values. In the spatial dimension along the x-axis and y-axis, entropy tends to increase as the distance between evaluated pixels increases, indicating greater unpredictability or randomness in grayscale variations at greater distances for both WT and HPP images. Within the polarization and diagonal axis, the entropy values of the WT image are higher than the HPP image especially after 100°(offset>10), reflecting the disorderliness or lack of specific patterns linked to polarization direction or alignment in HPP samples.

Correlation has a range of [-1, 1], with values close to either end indicating a perfectly positively or negatively correlated image. In the spatial dimension, as the distance between evaluated pixels increases along the x-axis and y-axis, correlation values generally decrease. In WT images, we observe a linear decay in correlation as we move away from the pixel of interest across all angles of light. In the polar dimension, the HPP images tend to have larger correlation values (blue line) and exhibit more significant changes than the WT images as the evaluation distance increases. Intriguingly, the difference between polar vs. diagonal is smaller in WT images than HPP, which might suggest that WT images have more similar gray-level pairs regardless of the light's orientation.

In summary, spGLCM suggests a more well-defined collagen orientation in the WT than the HPP bone (Fig. 5). To further explore the collagen alignment, we explored collagen orientation distributions. We applied a FFT on polarization averaged WT and HPP SHG images and showed the radial sum intensities for 360° around the center of the FFT image for an example image (Fig. 5(A)-(B)). We found that for this HPP image, the prominent peaks except four axes (90°, 180°, 270°, 360°) are seen at 30° and 210°, in accord with the original SHG and FFT image [34]. We created a flow map of (I, φ), represented as vectors colored with I and oriented with φ, and found the WT bone image displays groups of fibers as well as a dominant orientation for the field of view (Fig. 5(C)) [35]. This Fourier space analysis supports our observations that the HPP bone has less well-defined regions of similar collagen orientations (Fig. 5(D)). We selected a subregion (100*100 pixel) per image from a subset of WT and HPP images (10 images per group) and found that for most subregions collagen fibers in WT and HPP tend to form along a dominant orientation, but in some images in HPP the collagen fibers were found to be oriented to more than one direction in the representative subregion (Fig. 5(E)-(F)).

3.5. Machine learning classification

spGLCM analysis provides a rich data set for the comparison between healthy and diseased bone collagen organization for machine learning. There is substantial variability within the populations, so individual features did not show statistical significance although they exhibited trends in previous figures. To synthesize this broad range of parameters into a description of the impact of HPP on bone collagen organization, we trained random forest and XGBoost using 121 spGLCM features where 80% of the data was used for training and 20% for validation. The ROC curve in Fig. 6(A) shows the True Positive Rate (Sensitivity) versus the False Positive Rate (1 - Specificity) for the RandomForest and XGBoost models after 5-fold cross-validation. The RandomForest model achieves a higher AUC-ROC score and an F1 score of 92.30%, outperforming XGBoost, which has an F1 score of 84.62% (Fig. 6(B)). Despite greater variability, random forest consistently demonstrates higher sensitivity and a better balance between sensitivity and specificity, indicating its superior overall performance. Confusion matrices and feature importance plots are shown in Supplement 1 S4 to illustrate the sensitivity and specificity of the two classification models. In the random forest model, we next explored features of importance to classification, and found that polar energy, contrast, homogeneity, entropy and correlation

Biomedical Optics EXPRESS

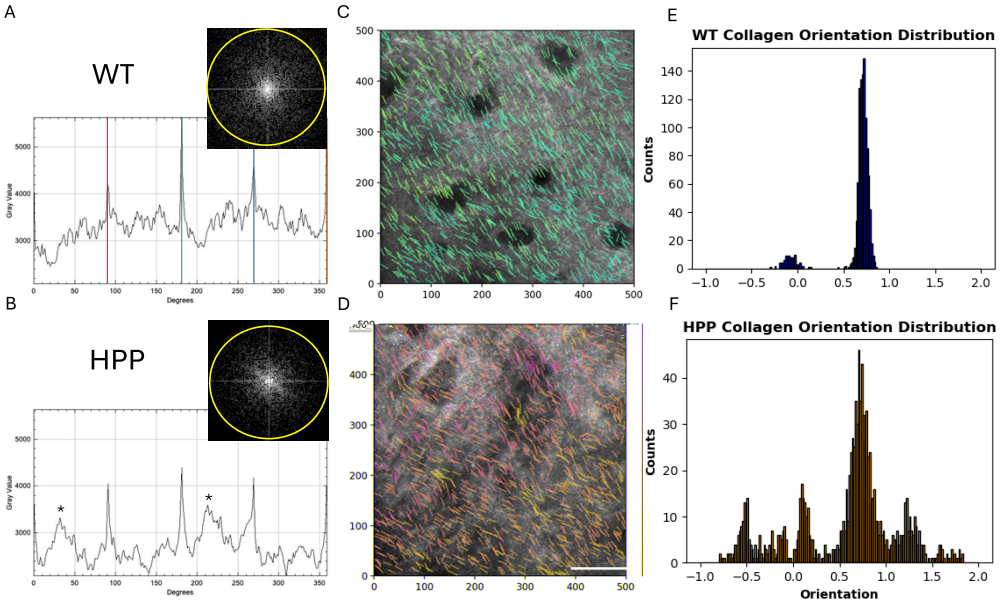

Fig. 5. (A-B) FFT intensity spectrum and radium sum intensity for WT and HPP sample. The radial sum intensities for 360 angles around the center of WT FFT image are plotted as an x-y scatter graph. The peaks at 90°, 180°, 270°, and 360° are from the axes of the FFT itself, show as red, green, blue and brown lines. Prominent peaks (black stars) are seen at 30° and 210°, in accord with the original HPP image and FFT image. (C-D) Flow map of (I, φ) represented as vectors coloured with I and oriented with φ, superimposed to the intensity image in grey. (E-F) Collagen orientation distribution of WT and HPP.

effectively describe the texture within the juvenile cranial bone. These spGLCM parameters find similar orientations of collagen that can help describe subtle differences in the collagen packing and alignment that might be otherwise missed.

We next investigated the importance of each feature, using an accepted metric known as the mean decrease in impurity [36], which is computed as the mean and standard deviation of accumulation of the impurity decrease within each tree. (Fig. 6(C)). We find energy along polar axis with larger offset are heavily weighted for the machine learning models, indicating the uniformity or periodicity in the structure are different between WT and HPP. Overall, these well-established machine learning models on the pSHG imaging data set suggest that expanding analysis to include polarimetric data with spGLCM features can more effectively categorize unknown samples into WT or HPP bone using differences in the collagen architecture associated with the HPP phenotype.

Biomedical Optics EXPRESS

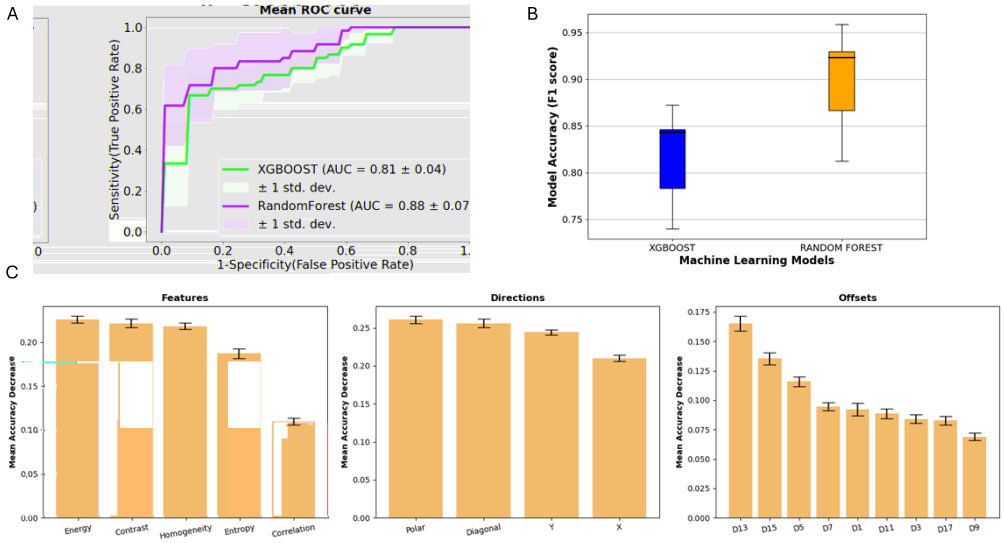

Fig. 6. Machine learning classification results. A. Mean ROC curve after 5-fold cross validation. B. spGLCM random forest found the highest F1 score of 92.30%±3.11% in the test data sets for correctly identifying WT and HPP bone. C. Importance of all features based on mean decrease in impurity.

4. Discussion

Polarization-resolved SHG is a label-free, non-destructive method of analyzing collagen structure that has been used in many tissues to describe disease states [37–39]. These range from direct mutations of collagen structure such as occur in osteogenesis imperfecta [37] to increases in collagen production caused by tumor formation [38] to collagen organization and remodeling during cervical ripening [40]. Our work applies polarization-resolved SHG to investigate the impact of defective mineral deposition in the bone on collagen assembly using a HPP mouse model. HPP is a debilitating disease that is defined by a mutation in the TNALP enzyme that dramatically reduces mineralization of the bones and teeth [41]. It is well established that the collagen-mineral interface changes the mechanical properties of bone [5,42,43], though this interface is poorly understood. Complementary to existing literature on collagen formation that has focused on the putative role of water to stabilize collagen structures and hydrogen bonding [44–46], our work supports the role of mineral in stabilizing collagen macrostructures observed in prior studies that have found mineral nucleation and growth within immature collagen fibers. This process compresses the collagen molecules along their triple helix axis [47,48], thereby allowing space for mineral propagation and collagen assembly into sheets [49]. The SHG polarimetry used in this work visualizes the disruption of the collagen structure at both the fiber and lamella sheet level of organization. Our texture analysis method incorporates both spatial and polarimetric data to clearly differentiate between healthy and HPP bone by evaluating the structure of the collagen fibers along the polarization angle axis.

The current work extends our prior efforts to evaluate collagen formation in full-thickness bone [14]. Other bone studies have used polarized SHG analysis to explore collagen organization in different regions of sliced bone [50] and in response to disease [37], but here, we did not manipulate the bone and were still able to describe collagen organization in healthy and diseased states. Much of the previous SHG work has relied on comparison between forward and back generated SHG to directly study thin sections [29,51], or extract bulk optical parameters of thicker samples [52] . Our SHG collection is limited to epi-mode so we collect a combination

Biomedical Optics EXPRESS

of back-generated signal and forward-generated signal that has been back-scattered, which may reduce our sensitivity to collagen orientation in comparison to thin sections that are able to separate the forward and backward SHG. Optical properties of the cranial bone such as birefringence, diattenuation, and polarization crosstalk impact the accuracy of polarimetric measurements in thick tissue [53]. Our prior work found minimal effect of these parameters on polarimetric measures captured within the first scattering length of the cranial bone; therefore, in the current studies we imaged less than 15 μm deep [14]. Our findings reveal that the nonlinear susceptibility ratio $\rho \approx 1.2 \pm 0.04$ remains consistent up to a depth of 15 μm, compared to ratio values reported for collagen in the literature (~1.4 for hydrated collagen) [28], indicating minimal impact from imaging depth on pSHG measurements. Similar approaches to investigate collagen fiber alignment have leveraged the periodic arrangement common in collagen using Fourier based analysis of bone and other tissues [15,54,55], including work from our lab [14]. This is especially well suited to tissues like tendon and muscle that have highly periodic structures, but less so for bone where there are numerous orientations of collagen bundles. Texture analysis using has been used to describe age and disease related differences in tendon and pancreatic tissues with SHG [56], and some studies have explored the potential to combine polarimetry with texture analysis on resulting collagen orientation profiles [57–59]. Here, we build on these methods to develop a spGLCM approach that includes the spatial polarimetric response of collagen in describing diseased states in whole bone tissue. Our work shows how the lack of molecular scale mineralization found in HPP appears to be associated with disruption of larger collagen lamella sheet structures. Using our spGLCM method allows the inclusion of polarization information in epi-detected thick samples, which makes classification between healthy and HPP more accurate.

The fusion of spatial polarimetric gray-level co-occurrence matrix (spGLCM) analysis and machine learning reveals distinct patterns in bone collagen between healthy and hypophosphatasia (HPP) states. Our models, particularly random forest, highlight the significance of polar energy and contrast in categorizing these states. Random forest builds multiple decision trees, averaging their predictions to reduce overfitting, while XGBoost improves gradient boosting with parallel processing and tree pruning for higher accuracy. However, XGBoost can be more sensitive to unscaled features compared to random forest and requires careful tuning of hyperparameters, making it less robust. Additionally, the use of only 121 samples is insufficient for some machine learning techniques, which may be the primary cause of inaccuracy. To enhance performance and ensure consistent results, we employ a cross-validation strategy, providing a more reliable assessment of the models.

Our random forest model showcases the impact of polar energy in categorizing these states. The values for energy in the polar and diagonal dimension found the highest magnitude of difference between the WT and HPP data sets, and the highest value for mean accuracy decrease in our machine learning models, indicating the importance of this GLCM feature in capturing collagen alterations in HPP. GLCM energy represents the sum of squared elements, reflecting periodicity and variation of the uniformity within pixel samples of collagen in the HPP mice. A flat curve suggests regularity and periodicity, whereas a highly fluctuated energy curve indicates randomness. We found that HPP samples had varying differences in uniformity in comparison with WT, suggesting differences in collagen packing and organization. Our findings underscore the potential of spGLCM parameters in delineating subtle differences in collagen organization, highlighting the relevance of polarimetric data in understanding HPP-associated collagen architecture.

Taken together, this study finds that collagen fiber and lamella sheet assemblies are significantly impaired in the HPP bone. Both SEM and SHG data support previous studies that indicated impairment in HPP collagen structure within osteoid using histological methods [59]. Our work does not directly address the mechanical effects of collagen organization; but literature investigating a range of disease states with bone fragility phenotypes such as osteoporosis, diabetes

Biomedical Optics EXPRESS

and aging has found collagen structural defects to be associated with fragility [60–64], and that misalignment of collagen and hydroxyapatite impairs bone strength and mechanical function [65]. Although the bone fragility of HPP has a direct origination from reduced mineral deposition and resulting bone mineral density [66], impaired collagen organization may increase severity of the bone weakness phenotype resulting from HPP. Thus, not only does the hypomineralization directly weaken the bone, but the associated observed collagen deformations may further diminish bone tensile properties and toughness. Furthermore, although we did not investigate collagen organization in the other mineralized craniofacial tissues like the periodontal ligament (PDL), it is possible that the disrupted collagen assembly we observe in HPP plays a role in reducing the binding strength of the PDL and contributes to the intact tooth loss associated with even mild odontohypophosphatasia [67].

In the future, it would be of interest to investigate the impact of a mineralization rescuing treatment on the collagen disorder observed in HPP. This could be done by treating HPP mice with Strensiq, the synthetic bone-targeted alkaline phosphatase enzyme used in patients to treat HPP [22]. In addition, it is important to note that our study uses the severe infantile form of HPP and evaluates lamellar sheet formation at two weeks of age when disorganized regions still are prevalent even in healthy mice. Future studies could seek to understand the impacts of HPP on collagen structure in mature mice with more mild forms of the disease using an adult HPP murine model. Many HPP patients exhibit comparatively mild symptoms such as tooth loss, frequent fractures, or bone degradation and osteoporosis in mid-life [22,41,66] that may also have a collagen organization defect or collagen degradation associated with them. In addition, our current work focused on the calvaria of HPP bone, and future efforts may aim to incorporate analysis of long bone- and even extend the technique to investigate other metabolic bone disorders.

5. Conclusion

Our work presented here develops polarized SHG imaging together with a spGLCM texture analysis for evaluating collagen fibers and lamella sheet structures of the bone in both a healthy and diseased state. By using HPP as our disease model, our work supports the linkage between collagen and mineral within the bone to stabilize macro collagen structures. We found that collagen is organized into regions of similar orientation within healthy bone and these regions are diminished within HPP bone. Similarly, lamella sheets are clearly defined with one or two dominant angles of orientation within the WT bone, but the collagen fibers of HPP bone lack as clear of a dominant angle of orientation. We developed a texture analysis method that incorporates both spatial and polarimetric data to differentiate between healthy and HPP bone by evaluating the structure of the collagen fibers along the polarization angle axis, using several machine learning classification techniques. This method can be expanded to describe bone health as it relates to aging or other diseases like osteogenesis imperfecta; and may be complimentary to current bone analysis techniques such as bone mineral density. This could allow for additional guidance on treatment of HPP and other metabolic bone disease by monitoring the collagen response to therapy.

Funding. National Institutes of Health (R21EB027802); National Science Foundation (1706916, 2040118); Regenerative Engineering and Medicine Georgia Partners in Medicine; Soft Bones (Maher Family Research Grant).

Acknowledgments. T.Z. was involved in conceptualization, investigation, data analysis, project management, writing, writing. E.G.P. was involved in conceptualization, investigation, data analysis, project management, writing. R.P.B. was involved in investigation, data analysis, project management. A.D.M. was involved in investigation and project management. P.A.K was involved in investigation, experimental guidance, project management, analysis, and writing. L.J.M. was involved in conceptualization, investigation, experimental guidance, project management, analysis, and writing.

Disclosures. The authors declare no conflicts of interest.

Biomedical Optics EXPRESS

Data availability. Data underlying the results presented in this paper are not publicly available at this time but may be obtained from the authors upon reasonable request.

Supplemental document. See Supplement 1 for supporting content.

References

1. P. Campagnola, "Second harmonic generation imaging microscopy: applications to diseases diagnostics," Anal. Chem. **83**(9), 3224–3231 (2011).
2. J. Y. Rho, L. Kuhn-Spearing, and P. Zioupos, "Mechanical properties and the hierarchical structure of bone," Medical Engineering & Physics **20**(2), 92–102 (1998).
3. O. Iijima, K. Miyake, A. Watanabe, *et al.*, "Prevention of lethal murine hypophosphatasia by neonatal ex vivo gene therapy using lentivirally transduced bone marrow cells," Hum. Gene Ther. **26**(12), 801–812 (2015).
4. J. Ji, B. Bar-On, and H. Daniel Wagner, "Mechanics of electrospun collagen and hydroxyapatite/collagen nanofibers," J. Biomed. Mater. Res. **13**, 185–193 (2012).
5. S. R. Stock, "The mineral-collagen interface in bone," Stock Calcified Tissue International **97**(3), 262–280 (2015).
6. W. J. Landis, K. J. Hodgens, M. J. Song, *et al.*, "Aspects of mineral structure in normally calcifying avian tendon," J. Struct. Biol. **117**(1), 24–35 (1996).
7. T. Kirsch and M. Pfaffle, "Selective binding of anchorin CII (annexin V) to type II and X collagen and to chondrocalcin (C-propeptide of type II collagen) Implications for anchoring function between matrix vesicles and matrix proteins," FEBS Lett. **310**(2), 143–147 (1992).
8. L. N. Wu, B. R. Genge, and R. E. Wuthier, "Matrix vesicle enzymes in human osteoarthritis," Bone Miner. **17**(2), 247–252 (1992).
9. M. Bossi, M. F. Hoylaerts, and J. L. Millan, "Mammalian alkaline phosphatases are allosteric enzymes," J. Biol. Chem. **268**(34), 25409–25416 (1993).
10. F. Vittur, N. Stagni, L. Moro, *et al.*, "Alkaline phosphatase binds to collagen; a hypothesis on the mechanism of extravesicular mineralization in epiphyseal cartilage," Experientia **40**(8), 836–837 (1984).
11. A. K. Nair, A. Gautieri, S.-W. Chang, *et al.*, "Molecular mechanics of mineralized collagen fibrils in bone," Nat. Commun. **4**(1), 1724 (2013).
12. M. Kikuchi, S. Itoh, S. Ichinose, *et al.*, "Self-organization mechanism in a bone-like hydroxyapatite/collagen nanocomposite synthesized in vitro and its biological reaction in vivo," Biomaterials **22**(13), 1705–1711 (2001).
13. E. R. Wise, S. Maltsev, M. E. Davies, *et al.*, "The organic− mineral interface in bone is predominantly polysaccharide," Chemistry of Materials **19**, 5055–5057 (2007).
14. E. G. Pendleton, K. F. Tehrani, R. P. Barrow, *et al.*, "Second harmonic generation characterization of collagen in whole bone," Biomed. Opt. Express, **11**, 4379–4396 (2020).
15. R. Ambekar, M. Chittenden, I. Jasiuk, *et al.*, "Quantitative second-harmonic generation microscopy for imaging porcine cortical bone: comparison to SEM and its potential to investigate age-related changes," Bone **50**, 643–650 (2012).
16. T. Yasui, Y. Tohno, and T. Araki, "Determination of collagen fiber orientation in human tissue by use of polarization measurement of molecular second-harmonic-generation light," Appl. Opt. **43**(14), 2861–2867 (2004).
17. A Deniset-Besseau, J Duboisset, MC Benichou, *et al.*, "Measurement of the second-order hyperpolarizability of the collagen triple helix and determination of its physical origin," J. Phys. Chem. B **113**(40), 13437–45 (2009).
18. P. S. Henthorn, M. Raducha, K. N. Fedde, *et al.*, "Different missense mutations at the tissue-nonspecific alkaline phosphatase gene locus in autosomal recessively inherited forms of mild and severe hypophosphatasia," *Proceedings of the National Academy of Sciences of the United States of America*, 89, (1992), 9924–9928.
19. E. Mornet, "Hypophosphatasia," Orphanet Journal of Rare Diseases **2**(1), 40 (2007).
20. R. A. Sutton, S. Mumm, S. P. Coburn, *et al.*, ""Atypical femoral fractures" during bisphosphonate exposure in adult hypophosphatasia," Journal of Bone and Mineral Research, **27**, 987–994 (2012).
21. M. P. Whyte, in *Hypophosphatasia: Nature's Window on Alkalinephosphatase Function in Man*, R. L. Bilezikian and J. Rodan, eds. (Academic Press, 2002), pp.1229–1248.
22. M. P. Whyte, "Hypophosphatasia – aetiology, nosology, pathogenesis, diagnosis and treatment," Nat. Rev. Endocrinol. **12**(4), 233–246 (2016).
23. J. Liu, H. K. Nam, C. Campbell, *et al.*, "Tissue-nonspecific alkaline phosphatase deficiency causes abnormal craniofacial bone development in the alpl−/− mouse model of infantile hypophosphatasia," Bone **67**, 81–94 (2014).
24. T. Zheng, A. R. Liversage, L. J Tehrani, *et al.*, "Imaging mitochondria through bone in live mice using two-photon fluorescence microscopy with adaptive optics," Frontiers in Neuroimaging **2**, 959601 (2023).
25. X. Chen, O. Nadiarynkh, S. Plotnikov, *et al.*, "Second harmonic generation microscopy for quantitative analysis of collagen fibrillar structure," Nat. Protoc. **7**(4), 654–669 (2012).
26. R. Mercatelli, S. Mattana, R Capozzoli, *et al.*, "Morpho-mechanics of human collagen superstructures revealed by all-optical correlative micro-spectroscopies," Commun. Biol. **2**(1), 117 (2019).
27. C. Teulon, I. Gusachenko, G. Latour, *et al.*, "Probing the structure of collagen in tissues: forward versus backward polarization-resolved SHG microscopy," Opt. Express **23**(7), 9313–9328 (2015).
28. Hwanhee Jeon, MacAulay Harvey, Richard Cisek, *et al.*, "Characterization of pathological stomach tissue using polarization-sensitive second harmonic generation microscopy," Biomed. Opt. Express **14**(10), 5376–5391 (2023).

Biomedical Optics EXPRESS

29. MA Houle, CA Couture, F Bancelin, *et al.*, "Analysis of forward and backward second harmonic generation images to probe the nanoscale structure of collagen within bone and cartilage," J. Biophotonics **8**(11-12), 993–1001 (2015).
30. R. M. Haralick, K. Shanmugam, and I. Dinstein, "Textural features for image classification," IEEE Trans. Syst., Man, Cybern. **SMC-3**(6), 610–621 (1973).
31. T. Saitou, H. Kiyomatsu, and T Imamura, "Quantitative morphometry for osteochondral tissues using second harmonic generation microscopy and image texture information," Sci. Rep. **8**(1), 2826 (2018).
32. Raghu Ambekar, Tung-Yuen Lau, Michael Walsh, *et al.*, "Quantifying collagen structure in breast biopsies using second-harmonic generation imaging," Biomed. Opt. Express **3**(9), 2021–2035 (2012).
33. R. Mercatelli, T. Triulzi, R Pavone, *et al.*, "Collagen ultrastructural symmetry and its malignant alterations in human breast cancer revealed by polarization-resolved second-harmonic generation microscopy," J. Biophotonics **13**(8), e202000159 (2020).
34. SE Taylor, T Cao, J. Talauliker, *et al.*, "Objective morphological quantification of microscopic images using a fast Fourier transform (FFT) analysis," Curr. Protoc. Essent. Lab. Tech. **95**(Suppl 7), 1–12 (2013).
35. Y Wang, JY Zhang, R Xu, *et al.*, "Diagnosing temporomandibular joint disorders using second harmonic imaging of collagen fibers," J Biophotonics. **15**(10), e202200075 (2022).
36. L. Breiman, J. Friedman, C.J Olshen, *et al.*, *Classification and Regression Trees* (1st ed.) (Chapman and Hall/CRC, 1984).
37. O. Nadiarnykh, S. Plotnikov, W. A. Mohler, *et al.*, "Second harmonic generation imaging microscopy studies of osteogenesis imperfecta," J. Biomed. Opt. **12**(5), 051805 (2007).
38. K. R. Campbell, R. Chaudhary, J. M. Handel, *et al.*, "Polarization-resolved second harmonic generation imaging of human ovarian cancer," J. Biomed. Opt. **23**(06), 1 (2018).
39. E. Ralston, B. Swaim, M. Czapiga, *et al.*, "Detection and imaging of non-contractile inclusions and sarcomeric anomalies in skeletal muscle by second harmonic generation combined with two-photon excited fluorescence," J. Struct. Biol. **162**(3), 500–508 (2008).
40. S. Bancelin, A. Nazac, B. H. Ibrahim, *et al.*, "Determination of collagen fiber orientation in histological slides using Mueller microscopy and validation by second harmonic generation imaging," Opt. Express **22**, 22561–22574 (2014).
41. M. P. Whyte, F. Zhang, D. Wenkert, *et al.*, "Hypophosphatasia: Validation and expansion of the clinical nosology for children from 25 years experience with 173 pediatric patients," Bone **75**, 229–239 (2015).
42. S. Weiner and H. D. Wagner, "The material bone: structure-mechanical function relations," Annu. Rev. Mater. Sci. **28**(1), 271–298 (1998).
43. S. Weiner, W. Traub, and H. D. Wagner, "Lamellar bone: structure-function relations," J. Struct. Biol. **126**(3), 241–255 (1999).
44. S. K. Holmgren, L. E. Bretscher, K. M. Taylor, *et al.*, "A hyperstable collagen mimic," Chem. Biol. **6**(2), 63–70 (1999).
45. S. K. Holmgren, K. M. Taylor, L. E. Bretscher, *et al.*, "Code for collagen's stability deciphered," Nature **392**(6677), 666–667 (1998).
46. L. E. Bertassoni, J. P. Orgel, O. Antipova, *et al.*, "The dentin organic matrix – limitations of restorative dentistry hidden on the nanometer scale," Acta Biomater. **8**(7), 2419–2433 (2012).
47. S. Lees, L. C. Bonar, and H. A. Mook, "Possible effect between the molecular packing of collagen and the composition of bony tissues," Int. J. Biol. Macromol. **6**(6), 321–326 (1984).
48. E. D. Eanes, D. R. Lundy, and G. N. Martin, "X-ray diffraction study of the mineralization of turkey leg tendon," Calc. Tis Res. **6**(1), 239–248 (1970).
49. C. W. McCutchen, "Do mineral crystals stiffen bone by straitjacketing its collagen?" J. Theor. Biol. **51**(1), 51–58 (1975).
50. D. Rouède, E. Schaub, J.-J. Bellanger, *et al.*, "Determination of extracellular matrix collagen fibril architectures and pathological remodeling by polarization dependent second harmonic microscopy," Sci. Rep. **7**(1), 12197 (2017).
51. J. Caetano-Lopes, A. M. Nery, H. Canhão, *et al.*, "Chronic arthritis leads to disturbances in the bone collagen network," Arthritis Research & Therapy. **12**(1), R9 (2010).
52. R. Lacomb and O. Nadiarnykh, "Quantitative second harmonic generation imaging of the diseased state osteogenesis imperfecta: experiment and simulation," Biophysical J. **94**, 4504–4514 (2008).
53. K. F. Tehrani, E. G. Pendleton, W. Michael Southern, *et al.*, "Spatial frequency metrics for analysis of microscopic images of musculoskeletal tissues," Connect. Tissue Res. **62**(1), 4–14 (2021).
54. M. Sivaguru, S. Durgam, R. Ambekar, *et al.*, "Quantitative analysis of collagen fiber organization in injured tendons using Fourier transform-second harmonic generation imaging," Optics Express **18**, 24983–24993 (2010).
55. A. Ghazaryan, H. Tsai, G. Hayrapetyan, *et al.*, "Analysis of collagen fiber domain organization by Fourier second harmonic generation microscopy," J. Biomed. Opt. **18**, 031105 (2013).
56. W. Hu, H. Li, L. Fu, *et al.*, "Characterization of collagen fibers by means of texture analysis of second harmonic generation images using orientation-dependent gray level co-occurrence matrix method," J. Biomed. Opt. **17**, 026007 (2012).
57. A. Golaraei, L. B. Mostaço-Guidolin, V. Raja, *et al.*, "Polarimetric second-harmonic generation microscopy of the hierarchical structure of collagen in stage I-III non-small cell lung carcinoma," Biomed. Opt. Express **11**(4), 1851–1863 (2020).

Biomedical Optics EXPRESS

58. R. Hristu, L. G. Eftimie, B. Paun, *et al.*, "Pixel-level angular quantification of capsular collagen in second harmonic generation microscopy images of encapsulated thyroid nodules," J. Biophotonics **13**(12), e202000262 (2020).
59. Y. Dong, J. Qi, H. He, *et al.*, "Quantitatively characterizing the microstructural features of breast ductal carcinoma tissues in different progression stages by Mueller matrix microscope," Biomed. Opt. Express**8**, 3643–3655 (2017).
60. F. Barvencik, F. T. Beil, M. Gebauer, *et al.*, "Skeletal mineralization defects in adult hypophosphatasia–a clinical and histological analysis," Osteoporosis Int. **22**(10), 2667–2675 (2011).
61. M. Saito and K. Marumo, "Collagen cross-links as a determinant of bone quality: a possible explanation for bone fragility in aging, osteoporosis, and diabetes mellitus," Osteoporosis Int. **21**(2), 195–214 (2010).
62. A. A. Poundarik, P. C. Wu, Z. Evis, *et al.*, "A direct role of collagen glycation in bone fracture," Journal of the Mechanical Behavior of Biomedical Materials **52**, 120–130 (2015).
63. D. Vashishth, "The role of the collagen matrix in skeletal fragility," Current Osteo. Rep. **5**(2), 62–66 (2007).
64. P. Zioupos, J. D. Currey, and A. J. Hamer, "The role of collagen in the declining mechanical properties of aging human cortical bone," J. Biomed. Mater. Res. **45**(2), 108–116 (1999).
65. A. Sekita, A. Matsugaki, and T. Nakano, "Disruption of collagen/apatite alignment impairs bone mechanical function in osteoblastic metastasis induced by prostate cancer," Bone **97**, 83–93 (2017).
66. M. L. Bianchi, "Improving adherence to and persistence with oral therapy of osteoporosis," Osteoporosis international. **26**(5), 1629–1638 (2015).
67. T. van den Bos, G. Handoko, A. Niehof, *et al.*, "Cementum and dentin in hypophosphatasia," J. Dent. Res. **84**(11), 1021–1025 (2005).